
PERGAMON

Journal of the Mechanics and Physics of Solids
50 (2002) 955–977

JOURNAL OF THE
MECHANICS AND
PHYSICS OF SOLIDS

www.elsevier.com/locate/jmps

Size effects in the constrained deformation of metallic foams

C. Chen, N.A. Fleck*

Department of Engineering, University of Cambridge, Trumpington Street, Cambridge CB2 1PZ, UK

Received 2 August 2001; accepted 16 October 2001

Abstract

The constrained deformation of an aluminium alloy foam sandwiched between steel substrates has been investigated. The sandwich plates are subjected to through-thickness shear and normal loading, and it is found that the face sheets constrain the foam against plastic deformation and result in a size effect: the yield strength increases with diminishing thickness of foam layer. The strain distribution across the foam core has been measured by a visual strain mapping technique, and a boundary layer of reduced straining was observed adjacent to the face sheets. The deformation response of the aluminium foam layer was modelled by the elastic–plastic finite element analysis of regular and irregular two dimensional honeycombs, bonded to rigid face sheets; in the simulations, the rotation of the boundary nodes of the cell-wall beam elements was set to zero to simulate full constraint from the rigid face sheets. It is found that the regular honeycomb under-estimates the size effect whereas the irregular honeycomb provides a faithful representation of both the observed size effect and the observed strain profile through the foam layer. Additionally, a compressible version of the Fleck–Hutchinson strain gradient theory was used to predict the size effect; by identifying the cell edge length as the relevant microstructural length scale the strain gradient model is able to reproduce the observed strain profiles across the layer and the thickness dependence of strength.

Keywords: Metallic foams; Size effects; Strain gradient theory; Finite element method

1. Introduction

A wide range of metallic foams have become available recently. They offer the possibility of multi-functional use in sandwich panels, combining for example high bending stiffness and strength with good heat transfer capability, as reviewed in the recent monograph of Ashby et al. (2000). In conventional design with metallic foams,

* Corresponding author. Tel.: +44-1223-332-650; fax: +44-1223-332-662.
E-mail address: naf1@eng.cam.ac.uk (N.A. Fleck).

0022-5096/02/$ - see front matter
PII: S0022-5096(01)00128-4

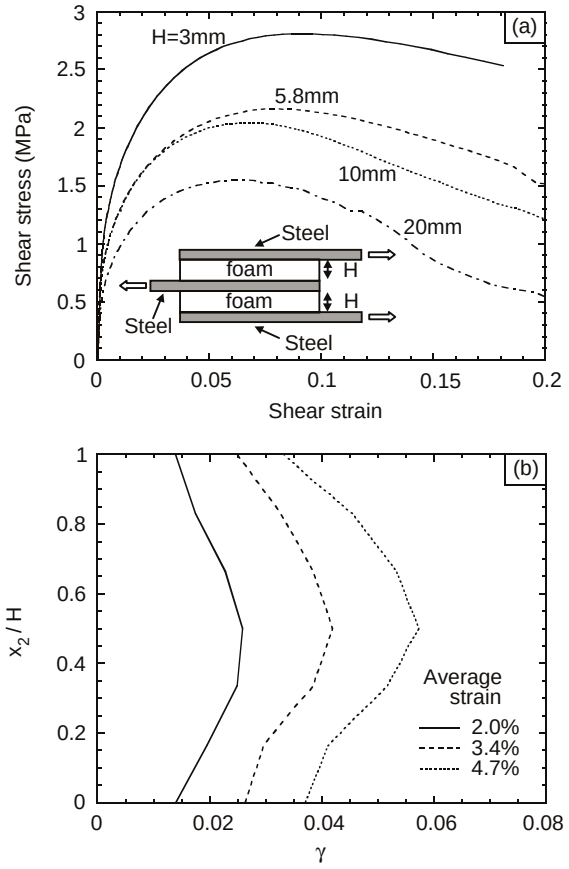

Fig. 1. (a) Effect of layer thickness upon the measured shear stress–strain response of Alporas foam, using the double lap shear geometry as shown in the inset; (b) through-thickness profile of shear strain, for a foam layer of thickness $H = 20$ mm.

they are idealised as an elastic–plastic compressible continuum, and the effects of a finite cell size upon the structural response are neglected. This approach is reasonable when the length scale of the structure is much greater than that of the microstructure. However, the cell size of commercially available metallic foams is in the range 1–10 mm, and it is common for the structural length scale (such as thickness of sandwich panel core) to be comparable with that of the cell size. For example, Chen et al. (2001) have manufactured sandwich beams with steel face sheets, and foam cores of thickness of 3–20 mm made from Alporas closed-cell aluminium alloy foam, of average cell size 3.5 mm (average cell edge length = 2 mm) and relative density 11%. They detected a size effect in shear, such that the shear strength of the foam core increased with diminishing thickness. The average (engineering) shear stress versus shear strain curves within each specimen are plotted in Fig. 1a, and clearly show that

the peak shear strength of the Alporas foam specimen with thickness $H = 3$ mm is about twice that of bulk Alporas foam. In the same set of experiments, but hitherto unpublished, the shear strain profile across the thickness of selected specimens was measured using a surface displacement analysis (SDA) method (Instron, Co., 1997). This involved video capture of the specimen at various stages of deformation, and then mapping of the shear strain distribution on the side face of the specimen. The shear strain was then averaged over the length of the specimen to minimise scatter, and the resulting total shear strain profile across the specimen thickness is shown in Fig. 1b for a representative specimen of thickness $H = 20$ mm, and overall average shear strains of 2.0%, 3.4% and 4.7%. It is clear that a boundary layer exists adjacent to each of the steel adherends.

Andrews et al. (2001) have observed a similar size effect in shear for Alporas foam provided the thickness is less than 12 mm (corresponding to about 3 times the cell size). They simultaneously varied the thickness and length of each specimen so that the aspect ratio of length/thickness was held fixed at 12. In contrast, the aspect ratio of the specimens tested by Chen et al. (2001) varied from 5 to 33 as the specimen thickness decreased from 20 to 3 mm. The agreement in magnitude of the size effect in both sets of experiment suggests that end effects are negligible in the experiments of Chen et al. (2001). The experimental investigation of Andrews et al. (2001) was supplemented by a theoretical study by Onck et al. (2001); they calculated analytically the shear strength (and stiffness) of a constrained regular honeycomb. An increase in shear strength was predicted when the thickness of the constrained layer was reduced to less than the cell height. In the present study, we show that a more pronounced size effect exists for irregular honeycombs.

In this study, an attempt is made to investigate size effects in the constrained deformation of a metallic foam layer, by experiment and by micromechanical and phenomenological modelling. First, an experimental investigation is reported on the plastic response of Alporas foam, sandwiched between two elastic steel plates and subjected to combined shear and through-thickness direct loading. Second, the observed size effect is modelled by two approaches: (i) a finite element simulation of the elastic–plastic deformation of a 2D honeycomb, and (ii) the elastic–plastic deformation response of a compressible version of the Fleck and Hutchinson (1997) strain gradient solid. In both analyses, the observed constraining effects of the elastic substrates upon the deformation of the sandwiched foam are predicted, and thereby a size effect is obtained.

2. Experimental study on the constrained deformation of Alporas foam

Combined shear and direct loading tests have been conducted on a sandwich layer of Alporas aluminium foam constrained between two steel plates in order to explore the effect of specimen thickness upon the deformation response. Before we report on the combined loading tests, we summarise first the effect of thickness of foam layer upon its response in constrained compression.

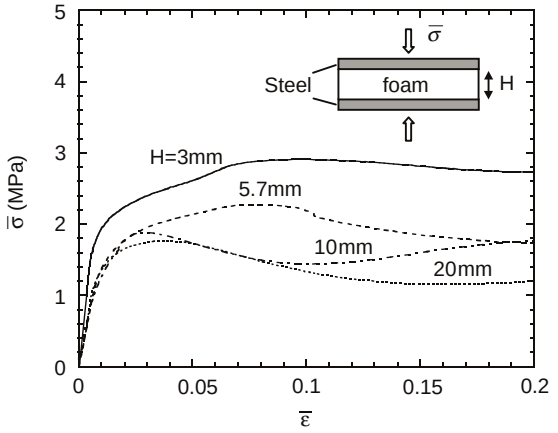

Fig. 2. Effect of layer thickness upon the compressive stress–strain response of Alporas foam in the through-thickness direction.

2.1. The compression response of a constrained foam layer

Sandwich plates with steel face sheets and an Alporas foam core have been manufactured and compressed in through-thickness direction, as follows. Alporas foam of relative density $10.7\% \pm 0.3\%$ was electro-discharge machined into rectangular plates of dimension 100 mm × 100 mm, and thickness in the range 3–20 mm; the plates were then bonded between two mild steel plates of thickness 10 mm using Redux 322 epoxy adhesive in an air-oven at 175°C for 2 h. Since the strength of Redux 322 epoxy is an order of magnitude greater than that of Alporas foam no adhesive failure occurred during any of the subsequent tests. The compression tests were performed using a conventional screw-driven test machine, so that the imposed average strain rate was $10^{-3}\ s^{-1}$. The nominal stress $\bar{\sigma}$ and the average nominal strain $\bar{\varepsilon}$ are plotted in Fig. 2.

It is noted that the uniaxial yield strength for the Alporas foam of thickness $H = 20$ mm is about 1.8 MPa, consistent with that reported by Harte et al. (1999) for the yield strength of bulk Alporas foam. A clear size effect is observed in constrained compression, with the strength increasing with diminishing thickness of foam layer. The overall magnitude of the size effect is comparable to that shown in Fig. 1a. We argue that this size effect is not associated with the changing aspect ratio of the sandwich layer and any attendant plastic constraint effects: Deshpande and Fleck (2000) have found that the 'plastic Poisson ratio' for this foam is almost zero, and so a state of through-thickness uniaxial strain does not induce in-plane stresses within the foam layer. Instead, it is argued that the size effect in constrained through-thickness compression of the foam is due to the development of a boundary layer adjacent to the steel plates: the epoxy adhesive provides local reinforcement of the cell walls against rotation

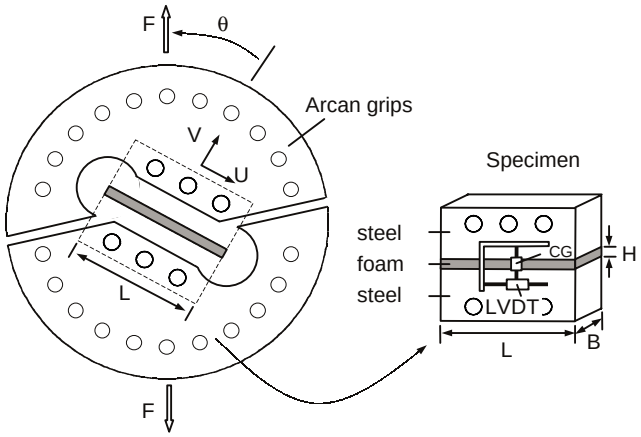

Fig. 3. Sketch of the Arcan test grips and specimen.

2.2. The constrained response of a foam layer under combined shear and tension

Alporas foam plates of length $L = 74$ mm, width $B = 19$ mm and thicknesses $H = 3$ and 10 mm were machined from as-received blocks, and were then hot-bonded using Redux 322 epoxy adhesive to two steel loading plates of an Arcan test fixture (Arcan et al., 1978), as sketched in Fig. 3. In each test the applied traction on the top and bottom faces of the specimen was along a fixed direction θ by suitable adjustment of the orientation of the test fixture within the loading train of the screw-driven test machine. For example, for a loading angle $\theta = 0^\circ$, the specimen was subjected to tension in the through-thickness direction, while for $\theta = 90^\circ$, the specimen was subjected to simple shear. Intermediate values of loading angle θ gave rise to a combined shear-tension proportional loading. The relative shear U and normal displacement V over the thickness of the specimens were recorded using a linear variable differential transformer (LVDT) and a clip gauge (CG), respectively, as shown in Fig. 3. The average values of stress and strain components in the Alporas foam layer were calculated as follows. The normal and shear stresses are related to the applied load F by $\bar{\sigma} = F\cos\theta/LB$ and $\bar{\tau} = F\sin\theta/LB$, respectively, whilst the average nominal values of normal and shear strains are given by $\bar{\varepsilon} = V/H$ and $\bar{\gamma} = U/H$, respectively.

A series of tests has been conducted for specimens of thickness H=3 and 10 mm, and for the loading angles θ=0°, 15°, 45°, 60° and 90°, at a strain rate of about 10^{-3} s^{-1}. Selected tests were repeated and confirmed that the measured stress–strain curves are repeatable to within about 10% in stress level at any given strain. Typical results for various loading angles θ and for both values of specimen thickness H are summarised in Fig. 4; the shear stress versus shear strain curves are given in Fig. 4a, whilst for the same specimens the through-thickness stress versus strain responses are shown in Fig. 4b. It is seen from Fig. 4 that the foam layer first deforms elastically, followed by a hardening plastic response. After a few percent of macroscopic straining (ranging from 2% to 6%, depending upon the value of the loading angle θ), distributed microcracking

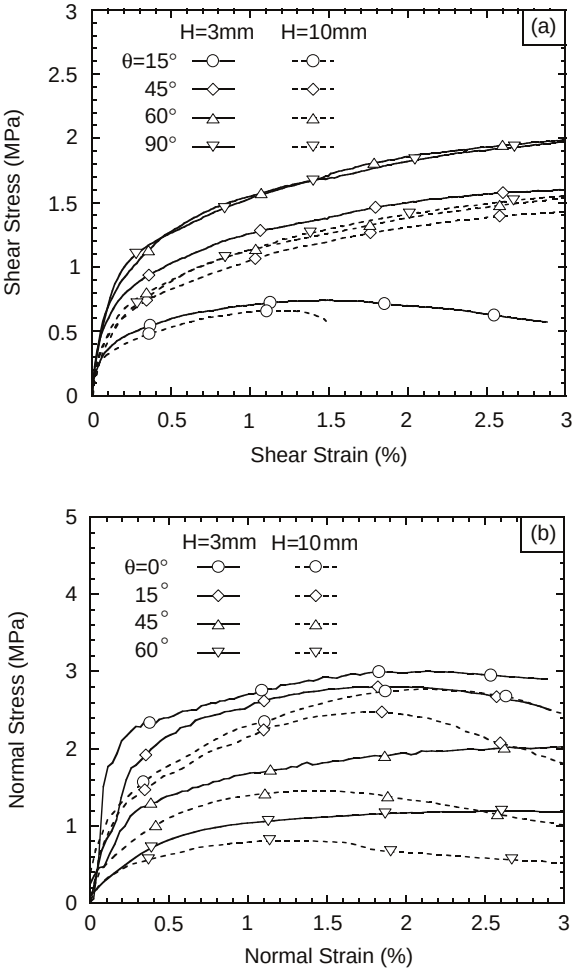

Fig. 4. The measured average stress–strain curves for Alporas foam layers of thickness $H = 3$ and 10 mm: (a) shear stress–strain curves, and (b) tensile stress–strain curves. The foam layer is subjected to through-thickness tension ($\theta=0^\circ$), to simple shear ($\theta=90^\circ$), and to combined tension and shear ($\theta=15^\circ$, 45°, and 60°).

occurs and the measured stress starts to drop. For all loading angles a size effect is observed: the shear and normal strengths for the 3 mm thick foam consistently exceed the corresponding values for the 10 mm thick layer.

The measured stress versus strain curves for $H=3$ and 10 mm were used to construct the initial yield surface in $(\bar{\sigma}$–$\bar{\tau})$ space, see Fig. 5. Here, the initial yield strength has been defined at an offset strain of 0.2% on the normal stress versus normal strain curves; the corresponding shear strength is calculated from the known direction of overall traction on the specimen. The yield surfaces are geometrically self-similar, and their elliptical shape supports the Deshpande and Fleck (2000) flow theory description

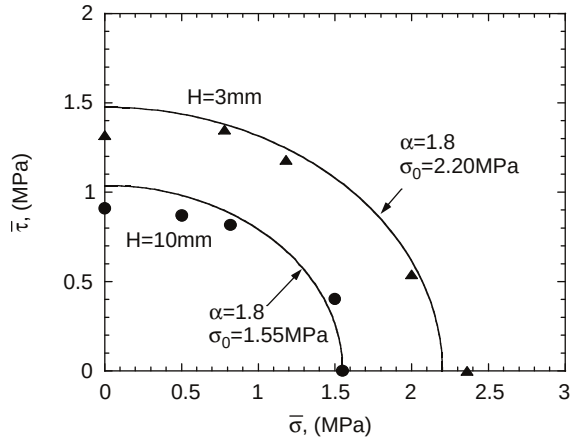

Fig. 5. The measured initial yield loci in $\bar{\sigma}$–$\bar{\tau}$ space for Alporas foam layers of thickness $H = 3$ and 10 mm. Symbols denote experimental results whilst solid lines are curve fits using Eq. (2).

of metallic foams, summarised as follows. Deshpande and Fleck defined a combined loading parameter $\hat{\sigma}$ by

$$\hat{\sigma} \equiv \left[\frac{1}{1+\alpha^2/9}(\sigma_e^2 + \alpha^2\sigma_m^2)\right]^{1/2} \tag{1}$$

in terms of the von Mises effective stress $\sigma_e = \sqrt{3\sigma'_{ij}\sigma'_{ij}/2}$, and the mean stress $\sigma_m = \sigma_{ii}/3$, where σ_{ij} is the stress tensor, σ'_{ij} is the deviatoric stress, and a repeated suffix denotes a repeated sum from 1 to 3. The material parameter α denotes the ratio of deviatoric strength σ_e to hydrostatic strength σ_m, and the normalisation $1 + (\alpha^2/9)$ in Eq. (1) is included in the definition of $\hat{\sigma}$ so that it equals the uniaxial stress under uniaxial loading. Deshpande and Fleck (2000) assumed that yield occurs when $\hat{\sigma}$ attains the uniaxial yield strength σ_0. Associated plastic flow with isotropic hardening is adopted, and the hardening response is calibrated against that for a foam sample under uniaxial tension, or compression.

Consider the case of a constrained layer with rigid adherends. The ratio of in-plane dimension to layer thickness is taken to be sufficiently large that end-effects can be neglected, and in the absence of strain gradient effects, the stress state within the constrained is uniform. The presence of the adherends ensures that the in-plane strain components vanish, with finite values only for the through-thickness normal and shear strain components. Define $\bar{\sigma}$ as the through-thickness normal stress and $\bar{\tau}$ as the through-thickness shear stress within the constrained foam layer. Then, the Desphande–Fleck yield criterion (1) becomes

$$\hat{\sigma}^2 \equiv \frac{1}{1+(\alpha/3)^2}\left[3\bar{\tau}^2 + \frac{\alpha^2\bar{\sigma}^2}{1+(2\alpha/3)^2}\right] = \sigma_0^2 \tag{2}$$

which is evidently an ellipse in $(\bar{\sigma}$–$\bar{\tau})$ space. It is instructive to attempt a curve fit of Eq. (2) to the yield surface loci given in Fig. 5 for foam layers of thickness $H = 3$

and 10 mm, by treating α and σ_0 as material parameters for each thickness. In an independent experimental study Fleck et al. (2001) obtained the value $\alpha = 1.8$ for unconstrained large specimens of Alporas foam of relative density $\bar{\rho} = 11\%$. With this choice of eccentricity of ellipse Eq. (2) gives an adequate curve fit to the yield surface loci of Fig. 5, provided we take the uniaxial yield strength σ_0 of the foam to equal the bulk value of 1.55 MPa for $H = 10$ mm, and an elevated value $\sigma_0 = 2.20$ MPa for $H = 3$ mm. We emphasise that the conventional Deshpande–Fleck foam model is unable to predict the effect of specimen size upon the value of σ_0, and must rely upon experimental data for each thickness of constrained layer.

Next, a 2D micromechanical model of the foam is introduced in order to predict the shape and size of yield surface; then, in Section 4, the Fleck–Hutchinson strain gradient plasticity theory is extended to describe the observed size effect from a phenomenological point of view.

3. Numerical simulation of the size effects in foams

3.1. Finite element model

In this section, the finite element method is used to simulate the observed thickness-effect on the combined shear and through-thickness strength of a sandwiched foam layer. In order to achieve practical computer storage and run-times the 3D microstructure of the Alporas foam is mimicked by that of a 2D irregular honeycomb, with a typical example shown in Fig. 6a. Although the microstructures of irregular 2D honeycombs differ considerably from those of 3D metallic foams, it has already been established that analyses based upon the much simpler 2D honeycomb microstructures provide valuable insight into the elastoplastic properties of current commercial 3D foams (see, for example, Warren and Kraynik, 1987; Silva et al., 1995; Chen et al., 1999). Several morphologies of two dimensional random honeycombs are available, including Γ and δ Voronoi honeycombs, honeycombs with randomly broken cell walls and honeycombs with cell-wall misalignments (Silva et al., 1995; Chen et al., 1999; Zhu et al., 2001). As shown by Chen et al. (1999), irregular 2D honeycombs have quantitatively similar elastoplastic behaviours to those of 3D metal foams. In this study, we adopt an irregular honeycomb with cell-wall misalignments, and, for comparison purposes, a regular honeycomb.

The geometric relation between a regular honeycomb and an irregular honeycomb containing cell-wall misalignments is shown in Fig. 6b. The misalignments are introduced by displacing in random directions the nodes of a regular hexagonal honeycomb by a constant distance $\chi\ell$, where ℓ is the length of each side of the regular hexagonal honeycomb, and the fixed fraction χ specifies the magnitude of the misalignment. Thus, the co-ordinates (x_1, x_2) of a typical joint node of the regular honeycomb are shifted to (x_1', x_2'), according to

$$x_1' = x_1 + \chi\ell \cos\Omega,$$

$$x_2' = x_2 + \chi\ell \sin\Omega, \tag{3}$$

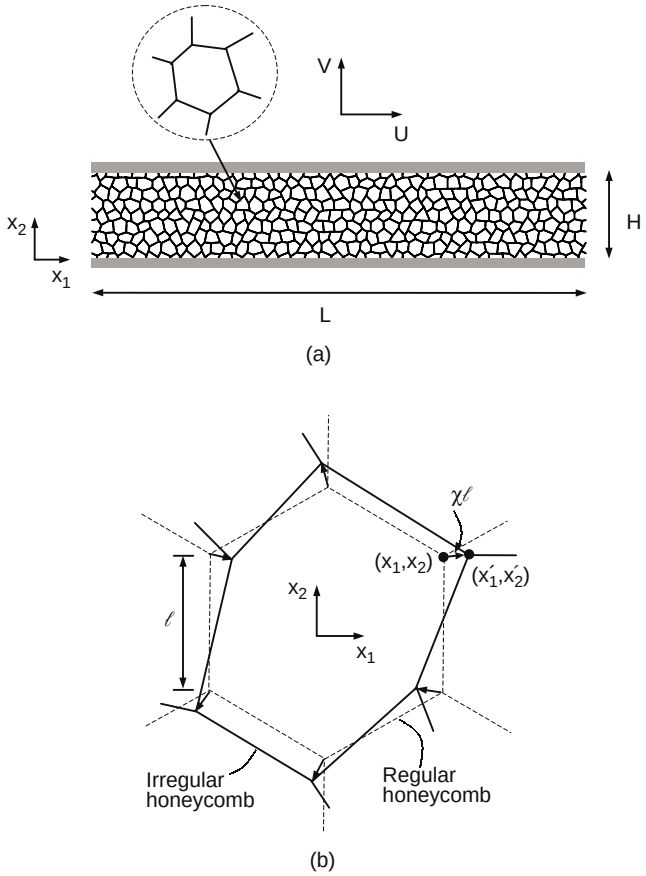

Fig. 6. (a) A typical finite element model for the foam layer modelled by an irregular 2D honeycomb with $\chi = 0.3$, and (b) a sketch showing the relation between a regular honeycomb and an irregular honeycomb.

where Ω is a *random* rotation from the x_1-axis. Chen et al. (1999) have shown that the hydrostatic and uniaxial strengths of the irregular honeycomb are comparable provided χ has a value of at least 0.3. Recall that the hydrostatic strength of metallic foams is close to their uniaxial strength, in sharp contrast to the regular hexagonal honeycomb for which the hydrostatic strength much exceeds the uniaxial strength. Thus, we make the choice $\chi = 0.3$ in order for the irregular honeycomb to mimic the character of metallic foams; this degree of imperfection is illustrated in Fig. 6a. The cell walls of the honeycombs are taken as elastic-ideally plastic with a yield strain $\varepsilon_Y = \sigma_{CY}/E_C = 0.2\%$, where σ_{CY} is the yield strength and E_C is the Young's modulus of the cell wall material. The relative density is taken to be $\bar{\rho} = 5\%$, where the relative density is related to the average cell edge length ℓ and wall thickness t by $\bar{\rho} \approx 2t/(\sqrt{3}\ell)$. We note in passing that the relative density of the regular (and irregular) honeycombs was sufficiently high for plastic collapse to occur prior to elastic buckling under all stress states investigated.

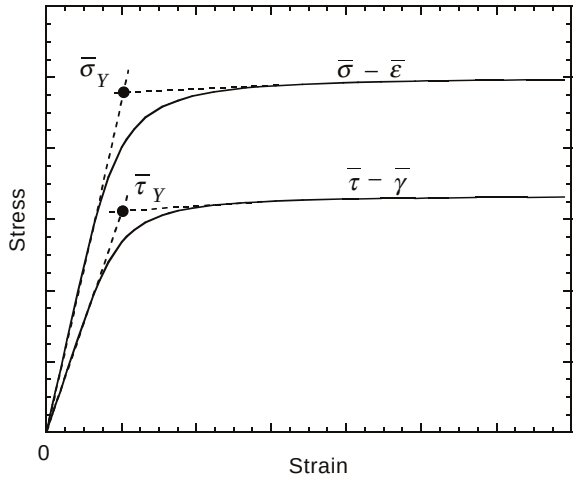

Fig. 7. Typical shapes of the shear stress–strain curve and the compressive stress–strain curve as predicted by finite element simulations of the irregular honeycomb.

In the finite element models, each cell wall is represented by 1 to 13 Timoshenko beam elements (element type B22 in ABAQUS), depending upon the ratio of cell wall thickness to cell edge length. A mesh sensitivity study has been performed to ensure that the meshes are sufficiently fine to ensure convergence. As shown in Fig. 6a, the relative horizontal displacement U and vertical displacement V are prescribed along the top and bottom faces. The presence of the rigid top and bottom adherends gives rise to additional kinematic constraints: the boundary nodes along the top and bottom of the finite element mesh are subjected to zero rotation. Periodic boundary conditions are applied to the lateral boundaries, with proportional straining enforced for numerical convenience. We limit our simulations to shear loading and through-thickness compression, and omit the case of through-thickness tension: numerical experimentation reveals that the yield point for through-thickness tension is equal in magnitude to that of through-thickness compression, but subsequent strong geometric hardening makes the tensile yield point difficult to identify. A detailed comparison of the predicted tensile and compressive stress–strain responses for regular and irregular honeycombs has been given previously by Chen et al. (1999).

3.2. Numerical results

The structural response of the foam layer is characterised by the ratio H/ℓ in addition to the relative density of the foam. In the finite element simulations of the irregular foam, six realisations of the random microstructure were generated using $\chi = 0.3$ and a uniform dispersion of Ω, and the results for average stress and strain were ensemble-averaged in order to minimise scatter. The ensemble-averaged shear stress versus shear strain curve ($\bar{\tau}$–$\bar{\gamma}$) and ensemble-averaged normal stress versus strain curve ($\bar{\sigma}$–$\bar{\varepsilon}$) are given in Fig. 7, where the macroscopic average stresses and

strains are defined by

$$\bar{\tau} = F_1/(LB), \quad \bar{\gamma} = U/H,$$
$$\bar{\sigma} = F_2/(LB), \quad \bar{\varepsilon} = V/H. \tag{4}$$

Here, F_1 and F_2 are the shear and normal components of force on the foam layer; they are work conjugates to the applied displacements U and V, respectively. Although the cell walls comprise elastic-ideally plastic material, the macroscopic response of the foam is characterised by a smooth transition from elastic to plastic flow, with a small degree of geometric hardening following yield. The initial yield strengths ($\bar{\sigma}_Y$ and $\bar{\tau}_Y$) are defined by a back extrapolation method, as sketched in Fig. 7: yield is taken as the intersection point between the linear elastic and the linear hardening curves.

The dependence of the shear and normal yield strengths ($\bar{\tau}_Y$ and $\bar{\sigma}_Y$) on the ratio of layer thickness H to microstructural length scale ℓ is shown in Fig. 8, where the normalising values τ_Y^0 and σ_Y^0 are the unconstrained shear and uniaxial strengths of a regular honeycomb (Gibson and Ashby, 1997),

$$\tau_Y^0 = \frac{\sqrt{3}}{8}\sigma_{CY}\bar{\rho}^2, \text{ and } \sigma_Y^0 = \frac{1}{2}\sigma_{CY}\bar{\rho}^2. \tag{5}$$

For comparison purposes, the yield strength has also been calculated for constrained layers of thickness H made from regular honeycombs. The orientation of the regular hexagonal honeycombs is shown in Fig. 6b, with the x_2-axis along the through-thickness direction of the foam layer. It is seen from Fig. 8 that a negligible size effect exists for the constrained shear and normal strengths of a regular honeycomb [1]; whilst the constrained shear strength is similar to the bulk value ($\bar{\tau}_Y \approx \tau_Y^0$), the constrained uniaxial yield strength much exceeds that of the bulk ($\bar{\sigma}_Y \gg \sigma_Y^0$). This can be understood as follows. The strain state within the constrained layer comprises uniaxial straining; the corresponding through-thickness strength $\bar{\sigma}_Y$ can be inferred from the available yield surfaces for regular and irregular honeycombs (Gibson and Ashby, 1997; Chen et al., 1999) by assuming associated plastic flow. An examination of the yield surface of regular hexagonal honeycombs (see Fig. 4.32 of Gibson and Ashby, 1997) reveals that the loading point for uniaxial compressive straining is at the vertex of the yield surface, corresponding to the hydrostatic strength, $\sigma_H^0 = 0.5\sigma_{CY}\bar{\rho}$. Therefore, the uniaxial yield strength of the foam when modelled by a regular honeycomb can be estimated as

$$\bar{\sigma}_Y/\sigma_Y^0 = \sigma_H^0/\sigma_Y^0 = 1/\bar{\rho} \tag{6}$$

which gives $\bar{\sigma}_Y/\bar{\sigma}_Y^0 = 20$ for the case $\bar{\rho} = 5\%$ as used in the present study. This estimate is in good agreement with the calculated value $\bar{\sigma}_Y/\sigma_Y^0 = 16$ in Fig. 8.

The through-thickness strength for uniaxial straining of the irregular honeycomb can be estimated in a similar manner. Since the yield surface of the bulk irregular honeycomb is nearly circular in deviatoric-mean stress space (Chen et al., 1999), its strength under all loading paths are similar in magnitude. Chen et al. (1999) further

[1] Onck et al. (2001) observed a similar behaviour for a regular honeycomb layer under constrained shear. An increase in shear strength with diminishing layer thickness was only detected for layers of thickness less than the cell height.

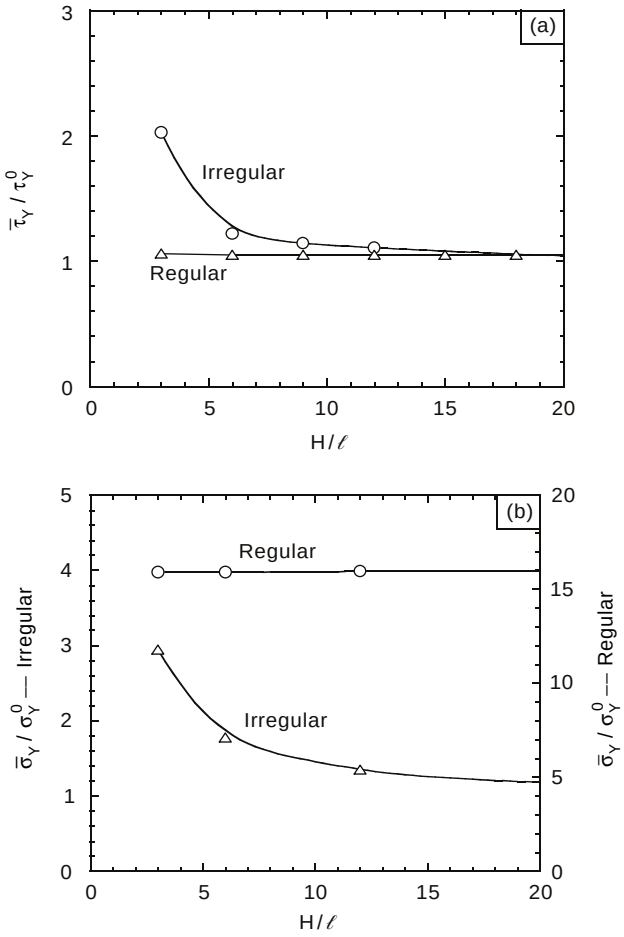

Fig. 8. Finite element predictions of the dependence of yield strength upon layer thickness H/ℓ for (a) shear strength, and (b) through-thickness compressive strength. Calculations have been performed for both regular and irregular honeycombs.

established that the uniaxial strength can be approximated by that of the associated regular hexagonal honeycomb σ_Y^0. Consequently, we expect $\bar{\sigma}_U \approx \sigma_Y^0$ when the foam is modelled by an irregular honeycomb with large H/ℓ. This argument is supported by the results shown in Fig. 8.

In contrast to the regular honeycomb, the irregular honeycomb displays a pronounced size effect in shear and normal strength for a constrained layer. Indeed, the size effect is comparable to that observed for Alporas foam: as H/ℓ is reduced from 20 to 3, the shear strength of the irregular honeycomb increases by a factor of about 2 and the normal strength by a factor of about 3. For the Alporas foam, the shear strength doubles when the layer height H is reduced from 20 to 3 mm, implying a value for the average cell edge length $\ell = 1$ mm in the finite element calculation. In reality, the

average cell edge length for the Alporas foam is about 2 mm. The discrepancy between measured and inferred values for ℓ is not surprising: a highly simplified 2D model has been used to represent the 3D closed cell foam.

It is instructive to explore the origin of the size effect by plotting the distribution of strain across the layer of irregular honeycomb. It is anticipated that the local strengthening against rotation of cell walls adjacent to the rigid adherends leads to the formation of a boundary layer of reduced strain. To check this hypothesis, the strain distribution across the layer has been calculated as follows, for selected cases. Denote the displacement components at a material point (x_1, x_2) of the foam by $u_k(x_1, x_2)$ where $k=1$ and 2. Since we are only concerned about the variation of the strain in the x_2-direction, the oscillations in $u_k(x_1, x_2)$ along the x_1 direction are smeared out by averaging u_k from $x_1 = 0$ to $x_1 = L$, to give

$$\bar{u}_k(\bar{x}_2) = \frac{1}{L}\int_0^L (u_k(x_1, x_2)\,\mathrm{d}x_1. \tag{7}$$

Thus, the local shear strain of interest is

$$\gamma = \mathrm{d}\bar{u}_1/\mathrm{d}x_2 \tag{8}$$

while the local normal strain of interest is

$$\varepsilon = \mathrm{d}\bar{u}_2/\mathrm{d}x_2. \tag{9}$$

The calculated distribution of strain components γ and ε for the irregular honeycomb layer under shear and uniaxial compression is plotted in Fig. 9. Results are given for the thicknesses $H/\ell = 6$ and 12, at an overall average shear strain and normal strain of 10%. It is seen that the local strain profiles capture the boundary layer effect, as shown in Fig. 1b from simple shear tests on Alporas foam. When the honeycomb is only about 2–3 cells thick (i.e. $H/\ell = 6$), the variation of local strains is approximately parabolic along the x_2: the local strains increase from the top and bottom layers and reach their peak values at mid-thickness. For a foam of thickness $H/\ell = 12$ the local strain distribution curves are much flatter at mid-thickness, with boundary layers of reduced straining adjacent to the rigid adherends. It is recalled that classical theories of continuum mechanics predict uniform distributions of strain under both simple shear and uniaxial loading. In order to capture the observed size effects and boundary layers, appeal must be made to higher order theories of plasticity involving higher order boundary conditions. In Section 4 below the phenomenological strain gradient theory of Fleck and Hutchinson (1997) is extended to predict size effects for metallic foams.

The initial yield locus has been determined from the finite element simulations of an irregular honeycomb layer for combined shear and through-thickness compression, with the choice $H/\ell = 3$, 6 and 12 as shown in Fig. 10. The shape of the yield surfaces is approximately elliptical, with no vertex formation, in agreement with the experimental results given in Fig. 5. As H/ℓ decreases from 12 to 3, the size of the yield surface increases in a self-similar manner by a factor of about 2. Recall that the measured yield surface of Fig. 5 also doubles when H is reduced from 10 to 3 mm, suggesting the

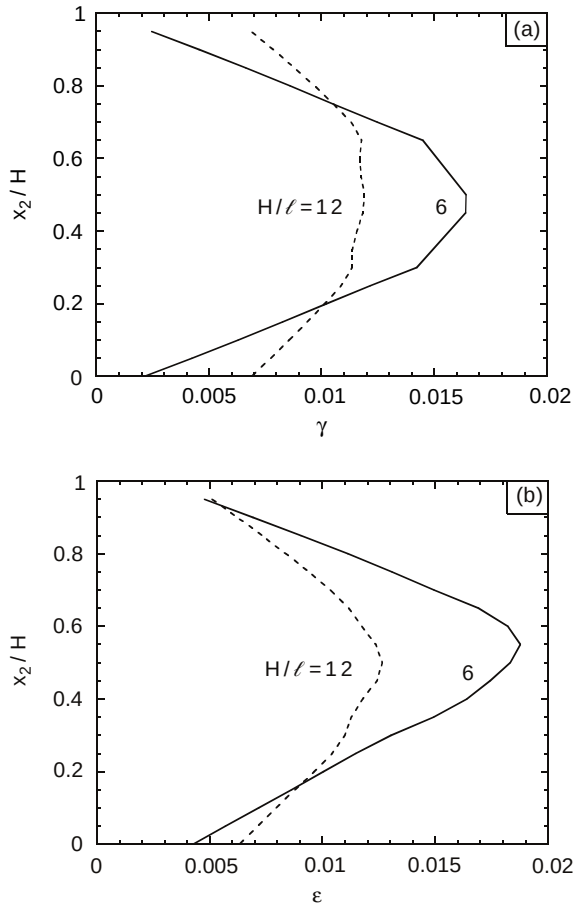

Fig. 9. Predictions of the local strain profile across the layer of an irregular honeycomb, for (a) shear and (b) compressive loading in the through-thickness direction. The layer thickness $H/\ell = 6$ and 12, and the average strain = 10% for both types of loading.

choice $\ell = 1$ mm as discussed above. Again this comparison implies that the average cell length of the Alporas foam (about 2 mm) is the relevant internal length scale for dictating the observed size effect.

4. Strain gradient plasticity predictions

Conventional theories of plasticity do not contain an internal material length scale; consequently, they are unable to predict a size dependence of strength. Several strain gradient theories of plasticity have been developed in recent years, each with the objective of predicting size effects at the micron scale (see, for instance, Aifantis, 1984; Muhlhaus and Aifantis, 1991; De Borst and Muhlhaus, 1992; Fleck and Hutchinson,

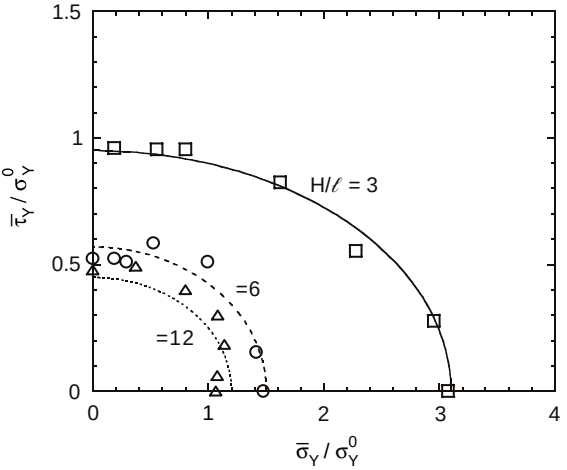

Fig. 10. Finite element predictions of the initial yield loci for an irregular honeycomb layer subjected to combined loading in $\bar{\sigma}$–$\bar{\tau}$ space.

1993, 1997, 2001; Gao et al., 1999; Gurtin, 1999). The phenomenological Fleck–Hutchinson theory (1997) was based on the physical notion that the strength of metals is elevated by the presence of geometrically necessary dislocations whose density scales with the first gradient of plastic strain. In the following section, we extend the deformation theory version of the Fleck–Hutchinson strain gradient theory to include the effects of plastic compressibility. The phenomenological theory is extended in such a manner that in the absence of strain gradients it gives the same response to proportional loading as that given by the Fleck and Deshpande (2000) flow theory for metallic foams. Then, we show that the modified strain gradient theory successfully predicts the size effects and boundary layer effect observed for Alporas foam, once we have identified the foam cell edge length as the microstructural length scale.

4.1. Extension of the Fleck–Hutchinson strain gradient theory for compressible solids

The Fleck and Hutchinson (1997) deformation theory version of strain gradient plasticity assumes that the strain energy density W is a scalar potential of an overall strain measure E_e; as originally conceived the solid is incompressible and E_e is defined as a quadratic measure of the deviatoric strain and deviatoric strain gradient,

$$E_e^2 = \frac{2}{3}\varepsilon'_{ij}\varepsilon'_{ij} + \sum_{I=1}^{3}[\ell_{(I)}^2 \eta_{ijk}^{(I)} \eta_{ijk}^{(I)}]. \tag{10}$$

Here, the summation convention over repeated indices applies, $\varepsilon'_{ij} = \varepsilon_{ij} - \delta_{ij}\varepsilon_{kk}/3$ is the deviatoric strain, and δ_{ij} is the usual Kronecker symbol. The length scales $\ell_{(I)}$ ($I = 1, 2,$ and 3) depend in some way upon microstructural features, and $\eta_{ijk}^{(I)}$ are the three orthogonal decompositions of the deviatoric strain gradient $\eta'_{ijk} = \eta_{ijk} - \eta_{ijk}^{H}$, where

$\eta_{ijk} = u_{k,ij}$ and $\eta^H_{ijk} = (\delta_{ik}\eta_{jPP} + \delta_{jk}\eta_{iPP})/4$. The full derivation of Eq. (10) is given in Fleck and Hutchinson (1997). No distinction is made between the plastic strain and the total strain since we are only interested in the deformation theory version for present purposes. A flow theory version can also be formulated along the lines laid down by Fleck and Hutchinson (1997), but this is omitted here for the sake of brevity.

Motivated by the study of Deshpande and Fleck (2000) on the multi-axial yielding of metallic foams, we modify the definition (10) of the overall strain E_e to

$$E_e^2 = \hat{\varepsilon}^2 + \hat{\eta}^2, \tag{11}$$

where $\hat{\varepsilon}$ is the scalar measure of strain introduced by Deshpande and Fleck (2000); it is related to the von Mises effective strain $\varepsilon_e = \sqrt{2\varepsilon'_{ij}\varepsilon'_{ij}/3}$ and to the volumetric strain $\varepsilon_m = \varepsilon_{ii}$ by

$$\hat{\varepsilon}^2 = (1 + \alpha^2/9)(\varepsilon_e^2 + \varepsilon_m^2/\alpha^2) \tag{12}$$

where α is a material constant, of order unity, for quantifying the degree of plastic compressibility. The strain gradient measure $\hat{\eta}$ on the right-hand side of Eq. (11) is that given by Wei and Hutchinson (1997),

$$\hat{\eta}^2 = \sum_{I=1}^{4} [\ell_{(I)}^2 \eta_{ijk}^{(I)} \eta_{ijk}^{(I)}], \tag{13}$$

where $\ell_{(I)}$ and $\eta_{ijk}^{(I)}$ $(I = 1, 2, 3)$ have already been defined in Eq. (10), and $\eta_{ijk}^{(4)} = \eta_{ijk}^H$ is the hydrostatic part of the strain gradient with accompanying length scale $\ell_{(4)}$.

On writing τ_{ijk} as the higher order stress, work conjugate to the strain gradient, and on defining an overall stress measure Σ as the work conjugate to E_e, we can state

$$\delta W = \Sigma \delta E_e = \sigma_{ij}\delta\varepsilon_{ij} + \tau_{ijk}\delta\eta_{ijk}. \tag{14}$$

It is convenient to employ the Smyshlyaev and Fleck (1996) unique orthogonal decomposition of third order tensors in order to re-write the higher order stress τ_{ijk} as the sum of its four orthogonal parts, $\tau_{ijk}^{(I)}$ $(I = 1, 2, 3,$ and $4)$. Note that the orthogonal decomposition for τ_{ijk} is identical to that used for η_{ijk}, and that each of the four quantities $\tau_{ijk}^{(I)}$ is work-conjugate to the respective strain gradient quantities $\eta_{ijk}^{(I)}$. Then, Eq. (14) leads to a direct connection between Σ and the generalised stress via

$$\Sigma^2 = \hat{\sigma}^2 + \hat{\tau}^2, \tag{15}$$

where $\hat{\sigma}$ has already been defined in Eq. (1), and

$$\hat{\tau}^2 = \sum_{I=1}^{4} \tau_{ijk}^{(I)} \tau_{ijk}^{(I)} / \ell_{(I)}^2. \tag{16}$$

Direct manipulation of (14) gives the connection between stress and strain quantities for the strain gradient deformation theory solid,

$$\sigma_{ij} = \frac{\Sigma}{E_e}\varepsilon_{ij} \text{ and } \tau_{ijk}^{(I)} = \frac{\Sigma}{E_e}\ell_{(I)}^2 \eta_{ijk}^{(I)} \quad \text{(no sum on } I\text{)}. \tag{17}$$

In uniaxial tension (or compression), Σ and E_e reduce to the uniaxial stress and strain components, respectively, and this allows for a simple experimental means of determining the hardening relation $\Sigma = \Sigma(E_e)$. The above theory reduces to the Fleck and Hutchinson (1997) deformation theory in the incompressible limit.

4.2. Prediction of the extended Fleck–Hutchinson theory in combined shear and tension

The compressible version of the Fleck–Hutchinson theory is now used to model the observed size effect in constrained metallic foam layers under combined shear and through-thickness tension. We simplify the problem to the 1D case where the displacement components u_1 and u_2 are functions only of x_2, as defined in Fig. 6a. Consequently, the non-vanishing strain and strain gradient components are

$$\gamma \equiv 2\varepsilon_{12} = u_{1,2}, \quad \varepsilon \equiv \varepsilon_{22} = u_{2,2},$$
$$\eta_1 \equiv \eta_{221} = u_{1,22}, \quad \eta_2 \equiv \eta_{222} = u_{2,22} \tag{18}$$

and the overall strain measure is re-written in the form

$$E_e^2 = A^2\gamma^2 + B^2\varepsilon^2 + C^2\eta_1^2 + D^2\eta_2^2, \tag{19}$$

where A and B are dimensionless constants, depending only upon the material compressibility parameter α, such that

$$A^2 = \frac{9+\alpha^2}{27}, \quad B^2 = \frac{(9+\alpha^2)(4\alpha^2+9)}{81\alpha^2}. \tag{20}$$

The parameters C and D have the dimension of length and are related to the internal length scales $\ell_{(I)}$ by

$$C^2 = \frac{4}{15}\ell_{(1)}^2 + \frac{1}{3}\ell_{(2)}^2 + \frac{2}{5}\ell_{(3)}^2,$$
$$D^2 = \frac{3}{5}\ell_{(1)}^2 + \frac{1}{48}\ell_{(2)}^2 + \frac{3}{40}\ell_{(3)}^2 + \frac{1}{2}\ell_{(4)}^2. \tag{21}$$

Thus, the role of the four internal length scales $\ell_{(I)}$ is replaced by that of two independent length scales C and D. In order to further specialise the strain gradient theory to the constrained foam problem, we introduce the stress measures ($\tau \equiv \sigma_{12}$, $\sigma \equiv \sigma_{22}, Q \equiv \tau_{221}$, $P \equiv \tau_{222}$) which are work-conjugate to $(\gamma, \varepsilon, \eta_1, \eta_2)$, respectively. Then, the overall stress measure Σ associated with the E_e can be expressed as

$$\Sigma^2 = \frac{\tau^2}{A^2} + \frac{\sigma^2}{B^2} + \frac{Q^2}{C^2} + \frac{P^2}{D^2} \tag{22}$$

and the stress–strain relations can be simplified to the form

$$\tau = \frac{\Sigma}{A^2 E_e}\gamma, \quad \sigma = \frac{\Sigma}{B^2 E_e}\varepsilon, \quad Q = \frac{\Sigma}{C^2 E_e}\eta_1, \text{ and } P = \frac{\Sigma}{D^2 E_e}\eta_2. \tag{23}$$

Note that only four stress measures are present in the constitutive law (23). The two governing equilibrium relations are

$$\tau_{,2} - Q_{,22} = 0, \tag{24}$$

$$\sigma_{,2} - P_{,22} = 0 \tag{25}$$

and these can be re-expressed in terms of the displacement components by making use of identities (18) and (23), to give

$$\frac{\Sigma(E_e)}{E_e} u_{1,2} - \frac{C^2}{A^2}\left(\frac{\Sigma(E_e)}{E_e} u_{1,22}\right)_{,2} = \frac{\bar{\tau}}{A^2}, \tag{26}$$

$$\frac{\Sigma(E_e)}{E_e} u_{2,2} - \frac{D^2}{B^2}\left(\frac{\Sigma(E_e)}{E_e} u_{2,22}\right)_{,2} = \frac{\bar{\sigma}}{B^2}, \tag{27}$$

where $\bar{\tau}$ and $\bar{\sigma}$ are the applied shear and normal tractions, respectively, on the top and bottom boundaries of the strip at $x_2 = 0, H$. The additional boundary conditions are

$$\text{On } x_2 = 0: \quad u_1 = u_2 = 0 \text{ and } \frac{\partial u_1}{\partial x_2} = \frac{\partial u_2}{\partial x_2} = 0,$$

$$\text{On } x_2 = H: \quad \frac{\partial u_1}{\partial x_2} = \frac{\partial u_2}{\partial x_2} = 0. \tag{28}$$

In general, the governing equations (26) and (27) have to be solved simultaneously; however, they can be reduced to a single non-linear ordinary differential equation upon making the following additional assumptions. Consider the case of proportional straining,

$$u_2 = \beta u_1 \tag{29}$$

with fixed β. Now invoke the additional constitutive assumption $A/B \equiv C/D$, which is consistent with the observation that the yield surfaces in Figs. 5 and 10 are geometrically self-similar. Then, the governing equation (27) becomes identically equal to (26) and we obtain

$$\frac{\bar{\sigma}}{\bar{\tau}} = \frac{\beta B^2}{A^2}. \tag{30}$$

Thus, proportional straining gives rise to proportional stressing.

It remains to calibrate the above phenomenological model with the material parameters α and $\Sigma(E_e)$. The value $\alpha = 1.8$ is taken from the experimental study of Fleck et al. (2001), while the strain hardening response $\Sigma(E_e)$ is determined from the measured shear stress–strain curve given in Fig. 1a for a specimen of thickness $H = 20$ mm; this thickness is sufficiently large for boundary layer effects to be negligible, as discussed in the introduction and by Andrews et al. (2001). The Ramberg–Osgood description,

$$\frac{\bar{\gamma}}{\gamma_0} = \frac{\bar{\tau}}{\tau_0} + \left(\frac{\bar{\tau}}{\tau_0}\right)^n \tag{31}$$

with $\gamma_0 = 0.106\%$, $\tau_0 = 0.533$ MPa and $n = 3.36$ provides an adequate fit to the data as shown by the comparison in Fig. 11a. For large specimens in simple shear we can

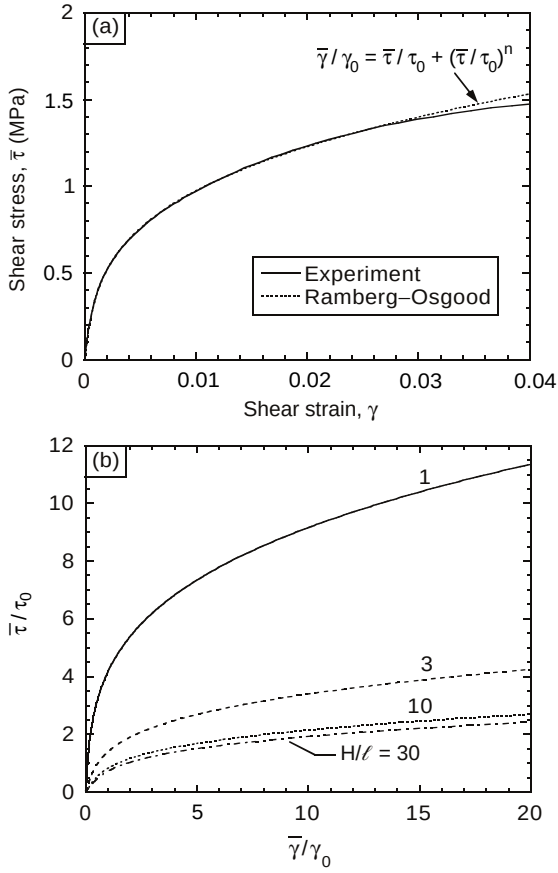

Fig. 11. (a) Calibration of the Ramberg–Osgood material description against the measured shear stress versus shear strain curve for the Alporas foam in simple shear with $H = 20$ mm; (b) Predicted average shear stress versus shear strain using the modified Fleck–Hutchinson strain gradient theory.

assume that $E_e = A\bar{\gamma}$ and $\Sigma = \bar{\tau}/A$ via Eqs. (19) and (22), respectively. Thus, the relation between Σ and E_e is stated as

$$\frac{E_e}{A\gamma_0} = \frac{\Sigma}{\tau_0/A} + \left(\frac{\Sigma}{\tau_0/A}\right)^n. \tag{32}$$

To complete the constitutive description, we assume that C/A equals the average cell edge length ℓ, with $A/B \equiv C/D$.

4.3. Numerical results

First, the effect of the foam layer thickness upon the shear response is calculated. A 1D finite element scheme has been employed to solve Eq. (26) in incremental fashion, using C1 continuous elements and a Hermite polynomial interpolation scheme for the

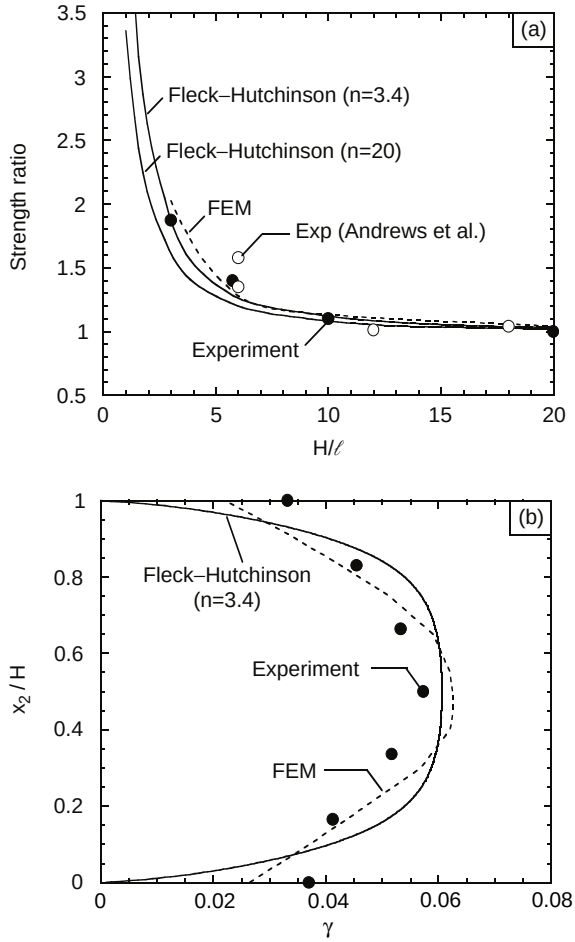

Fig. 12. Comparison of the measured and predicted size effect for a foam layer in simple shear: (a) effect of layer thickness upon strength. The experimental data of Andrews et al. (2001) are denoted by open symbols and the label 'Exp'; (b) the local shear strain profile at an average shear strain $\bar{\gamma} = 4.7\%$ and $H/\ell = 20$.

displacement field $u_1(x_2)$. The computed global shear stress–strain curves are shown in Fig. 11b for selected values of H/ℓ. A pronounced strengthening occurs when the thickness of the layer is comparable to that of the microstructural length scale ℓ. To investigate this further, a *strength ratio* at any given H/ℓ is defined as the shear traction at $\bar{\gamma}/\gamma_0 = 20$, normalised by its value in the absence of gradient effects (i.e. the shear traction at $\bar{\gamma}/\gamma_0 = 20$ in the limit $H/\ell = \infty$). The strength ratio is plotted against H/ℓ in Fig. 12a, for the Ramberg–Osgood fitted value of $n = 3.4$, and also for the much higher value $n = 20$ in order to represent the elastic-ideally plastic limit yet give numerical convergence. It is concluded that the effect of strain hardening upon the predicted strength ratio is minor according to the strain gradient theory.

It is instructive to add to Fig. 12a the measured strength data of the present study and those taken from Andrews et al. (2001). In both cases, we define the strength ratio as the peak shear strength normalised by the value at large H/ℓ, and choose the internal length scale ℓ to equal 1 mm in order to achieve a good fit to the Fleck–Hutchinson strain gradient theory with $n = 3.4$. Similarly, the strength ratio from the finite element simulations of a 2D irregular honeycomb is replotted in Fig. 12a by taking the values from Fig. 8a: again, the predictions are in close agreement with the observed strength ratios upon choosing the internal length scale ℓ to equal 1 mm.

The origin of the size effect is explored further by plotting in Fig. 12b the calculated and measured shear strain profiles across the layer. The comparison is made at an average strain of $\bar{\gamma}$=4.7%, with the choice H/ℓ=20 for the two methods of prediction. It is clear from Fig. 12b that a boundary layer exists in all 3 cases, although it is narrower in the two simulations than in the experiment. The Fleck–Hutchinson model takes as the higher order boundary condition the stipulation that the shear strain vanishes, as depicted in Fig. 12b. In contrast, the finite element simulations assume an elastic-ideally plastic response, with plastic hinge formation of the encastre cell edges adhered to the top and bottom adherends. Consequently, the shear strain within the homogenised layer remains finite along the upper and lower boundaries, see Fig. 12b. Similarly, the measured shear strain profile within the Alporas foam layer does not vanish at the rigid boundaries, and it is thought that this is also due to plastic hinge formation of the encastre cell edges. The significance of the higher order boundary conditions in the strain gradient and finite element simulations was explored by the following numerical experiment: a relaxation of the higher order displacement boundary conditions leads to a uniform distribution of shear strain across the layer and to a disappearance of the size effect.

A similar comparison of the computed and measured strength ratios can be made for through-thickness loading. The definition of strength ratio for through-thickness loading is analogous to that defined above for simple shear: the measured compressive strength, normalised by the strength at $H = 20$ mm, is plotted against H/ℓ in Fig. 13, with $\ell = 1$ mm. The predicted strength ratios are also given, and are taken directly from Figs. 8b and 12a for the finite element simulations and the modified Fleck–Hutchinson strain gradient theory, respectively. The strain gradient theory is able to capture the observed response, whilst the finite element simulations slightly overestimate the size effect for the assumed length scale $\ell = 1$ mm.

5. Concluding remarks

The effect of layer thickness upon the deformation of an Alporas foam layer has been examined experimentally and theoretically; the layer is constrained along its top and bottom faces by adhering it to two rigid loading plates. By varying the ratio of shear to through thickness direct stressing, a collapse surface for the foam has been measured: the magnitude of the size effect in constrained shear and through-thickness tension (and compression) are comparable.

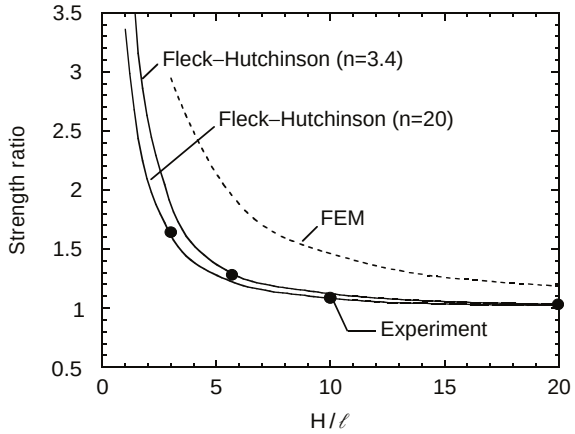

Fig. 13. Effect of layer thickness upon the measured and predicted strength ratio in through-thickness compression.

Two complementary strategies have been adopted in the numerical simulations: a micromechanical approach wherein the foam microstructure is simulated by 2D honeycombs, and a phenomenological approach using the Fleck and Hutchinson (1997) strain gradient theory, but extended with the aid of the Deshpande and Fleck (2000) constitutive description of metallic foams. Both models give remarkably similar predictions of the size effect, including the existence of a boundary layer of reduced straining adjacent to the rigid loading plates. By matching the predictions of both models to experiment the cell edge length is identified as the dominant microstructural feature associated with the size effect. The direct theoretical determination of the effective material length scale for a material containing a hierarchy of microstructural features remains a formidable task. Micromechanical methods show promise in making this connection, and recently notable progress has been made by a number of researchers including Drugan and Willis (1996) and Smyshlyaev and Cherednichenko (2000).

Acknowledgements

This work was supported by the EPSRC (UK) and by the DARPA/ONR (USA) MURI program on Ultralight Metallic Structures (No. N00014-1-96-1028). The authors are grateful to Anne-Marrie Harte, Robert Hutchinson, Craig Steeves, and Marc Zupan for their help in preparing the tests.

References

Aifantis, E.C., 1984. On the microstructural origin of certain inelastic models. ASME J. Eng. Mater. Tech. 106, 326–330.

Andrews, E.W., Gioux, G., Onck, P.R., Gibson, L.J., 2001. Size e in ductile cellular solids, Part II: experimental results. Int. J. Mech. Sci. 43, 701–713.

Arcan, M., Hashin, Z., Voloshin, A., 1978. A method to produce uniform plane-stress states with applications to fiber-reinforced materials. Exp. Mech. 18, 141–146.

Ashby, M.A., Evans, A.G., Fleck, N.A., Gibson, L.J., Hutchinson, J.W., Wadley, H.N.G., 2000. Metal Foams: a Design Guide. Butterworth Heinemann, Oxford.

Chen, C., Harte, A-M., Fleck, N.A., 2001. The plastic collapse of sandwich beams with a metallic foam core. Int. J. Mech. Sci. 43, 1483–1506.

Chen, C., Lu, T.J., Fleck, N.A., 1999. Effect of imperfections on the yielding of two-dimensional foams. J. Mech. Phy. Solids 47, 2235–2272.

De Borst, R., Muhlhaus, H.B., 1992. Gradient-dependent plasticity—formulation and algorithmic aspects. Int. J. Numer. Methods Eng. 35, 521–539.

Deshpande, V.S., Fleck, N.A., 2000. Isotropic constitutive models for metallic foams. J. Mech. Phys. Solids 48, 1253–1283.

Drugan, W.J., Willis, J.R., 1996. A micromechanics based nonlocal constitutive equation and estimates of the representative volume element size for elastic composites. J. Mech. Phys. Solids 44, 497–524.

Fleck, N.A., Hutchinson, J.W., 1993. A phenomenological theory for strain gradient effects in plasticity. J. Mech. Phys. Solids 41, 1825–1857.

Fleck, N.A., Hutchinson, J.W., 1997. Strain gradient plasticity. Adv. Appl. Mech. 33, 295–361.

Fleck, N.A., Hutchinson, J.W., 2001. An assessment of a class of strain gradient plasticity theories. J. Mech. Phys. Solids 49, 2045–2071.

Fleck, N.A., Olurin, O.B., Chen, C., Ashby, M.F., 2001. The effect of hole size upon the strength of metallic and polymeric foams. J. Mech. Phys. Solid 49, 2010–2030.

Gao, H., Huang, Y., Nix, W.D., Hutchinson, J.W., 1999. Mechanism based strain gradient plasticity—I. Theory. J. Mech. Phys. Solid 47, 1239–1263.

Gibson, L.J., Ashby, M.F., 1997. Cellular Solids: Structure and Properties, 2nd Edition. Cambridge University Press, Cambridge.

Gurtin, M.E., 1999. On the plasticity of single crystals: free energy, microforces, plastic-strain gradients. J. Mech. Phys. Solid 48, 989–1036.

Harte, A.M., Fleck, N.A., Ashby, M.F., 1999. Fatigue failure of an open cell and a closed cell aluminium alloy foam. Acta Mater. 47, 2511–2524.

Instron, Co., 1997. Surface displacement analysis software. Canton, MA 02021-1089.

Muhlhaus, H.B., Aifantis, E.C., 1991. A variational principle for gradient plasticity. Int. J. Solids Struct. 28, 845–857.

Onck, P.R., Andrews, E.W., Gibson, L.J., 2001. Size effects in ductile cellular solids. Part I: modeling. Int. J. Mech. Sci. 43, 681–699.

Silva, M.J., Hayes, W.C., Gisbon, L.J., 1995. The effect of non-periodic microstructure on the elastic properties of two-dimensional cellular solids. Int. J. Mech. Sci. 37, 1161–1177.

Smyshlyaev, V.P., Cherednichenko, K.D., 2000. On rigorous derivation of strain gradient effects in the overall behaviour of periodic heterogeneous media. J. Mech. Phys. Solid 48, 1325–1358.

Smyshlyaev, V.P., Fleck, N.A., 1996. The role of strain gradients in the grain size effect for polycrystals. J. Mech. Phys. Solid 44, 465–495.

Warren, W.E., Kraynik, A.M., 1987. Foam mechanics: the linear elastic response of two-dimensional spatially periodic cellular materials. Mech. Mater. 6, 27–37.

Wei, Y.G., Hutchinson, J.W., 1997. Steady-state crack growth and work of fracture for solids characterised by strain gradient plasticity. J. Mech. Phys. Solids 45, 1253–1273.

Zhu, H.X., Hobdell, J.R., Windle, A.H., 2001. Effects of cell irregularity on the elastic properties of 2D Voronoi honeycombs. J. Mech. Phys. Solids 49, 857–870.